3D tensor-based blind multi-spectral image decomposition for tumor demarcation

Ivica Kopriva* and Antun Peršin

Division of Laser and Atomic Research and Development, Ruđer Bošković Institute, Bijenička cesta 54, P.O. Box 180, 10002, Zagreb, Croatia

ABSTRACT

Blind decomposition of multi-spectral fluorescent image for tumor demarcation is formulated exploiting tensorial structure of the image. First contribution of the paper is identification of the matrix of spectral responses and 3D tensor of spatial distributions of the materials present in the image from Tucker3 or PARAFAC models of 3D image tensor. Second contribution of the paper is clustering based estimation of the number of the materials present in the image as well as matrix of their spectral profiles. 3D tensor of the spatial distributions of the materials is recovered through *3*-mode multiplication of the multi-spectral image tensor and inverse of the matrix of spectral profiles. Tensor representation of the multi-spectral image preserves its local spatial structure that is lost, due to vectorization process, when matrix factorization-based decomposition methods (such as non-negative matrix factorization and independent component analysis) are used. Superior performance of the tensor-based image decomposition over matrix factorization-based decompositions is demonstrated on experimental red-green-blue (RGB) image with known ground truth as well as on RGB fluorescent images of the skin tumor (basal cell carcinoma).

Keywords: 3D tensor, fluorescent multi-spectral image, data clustering, tumor demarcation.

1. INTRODUCTION

Increased occurrence of the skin cancer all over the world, [1], implies the large need for complementary methods for detection and accurate demarcation of skin cancers at an early stage to limit the damage caused by the tumors [2]. Photodynamic diagnoses (PDD) is a method for tumor demarcation that is based on the visualization of a fluorophore, with the ability to accumulate in tumor tissue, by the use of fluorescence imaging. Image decomposition methods widely used for the optical diagnoses, i.e. demarcation, are: ratio imaging [3,4], threshold based imaging, [2], as well as matrix factorization based methods [5]. Accuracy of first two groups of methods critically depends on the optimality of the threshold that up to some extent is always defined heuristically. Accuracy of the matrix factorization-based methods depends heavily on fulfillment of constraints imposed on spatial distributions of materials. Typical constraints are sparseness or statistical independence and they do not hold in a number of real world scenarios. To circumvent these difficulties 3D tensor factorization-based approach to unsupervised segmentation of the multi-spectral image has been proposed in [6]. Tensor of spatial distributions of the materials present in the image has been obtained by means non-negative tensor factorization (NTF) method that minimized α-divergence between original multi-spectral image tensor and its Tucker3 model [7,8]. Here, instead of performing computationally demanding NTF we propose a solution that estimates matrix of spectral profiles of the materials present in the image by means of clustering on *3*-mode matricized version of the original multi-spectral image. It is presumed that materials present in the image do not occupy the same pixel footprint. Under such assumption it is enough to randomly select small number of pixel indexes and then estimate the matrix of spectral profiles applying some standard data clustering method, such as *k*-means for example, on the selected pixel set. Tensor of spatial distributions of the materials present in the image is then obtained through *3*-mode multiplication of the original image tensor and pseudo-inverse of the estimated matrix of spectral profiles. This, tensor-based decomposition method is compared with matrix factorization methods on two experimental

* ikopriva@gmail.com; phone: +385 1 4571 286; fax: +385 1 4680 104

Medical Imaging 2010: Image Processing, edited by Benoit M. Dawant, David R. Haynor,
Proc. of SPIE Vol. 7623, 76231W · © 2010 SPIE · CCC code: 1605-7422/10/$18 · doi: 10.1117/12.839568

RGB images: the first one with simple structure and known ground truth and the second one that is fluorescent image of the skin tumor (basal cell carcinoma).

2. MATERIALS AND METHODS

For the segmentation purpose multi-spectral image is often represented in a form of the linear mixture model (LMM)

$$\mathbf{X}=\mathbf{AS} \tag{1}$$

where $\mathbf{X}\in R_+^{I_3\times I_1 I_2}$ represents multi-spectral image consisting of I_3 spectral bands and $I_1 I_2$ pixels, $\mathbf{A}\in R_+^{I_3\times J}$ represents matrix of spectral profiles of the materials present in the image (it is also known as mixing matrix) and $\mathbf{S}\in R_+^{J\times I_1 I_2}$ represents matrix of the J materials present in the image. R_+ is a real manifold with nonnegative elements. However, matrix factorization problem implied by linear mixture model (1) has infinitely many solutions unless additional constraints are imposed on model variables. This is due to the fact that representation (1) and representation $\mathbf{X}=\mathbf{ATT}^{-1}\mathbf{S}$ are equivalent from the data matrix $\mathbf{X}$ point of view, whereas $\mathbf{T}$ is any invertible matrix. Thus, infinitely many pairs ($\mathbf{A}$,$\mathbf{S}$) can give rise to $\mathbf{X}$. To achieve solutions which are meaningful, i.e. have physical interpretation, indeterminacies must be reduced to $\mathbf{TT}^{-1}=\mathbf{P\Lambda}$, whereas $\mathbf{P}$ is permutation matrix and $\mathbf{\Lambda}$ is diagonal matrix. These are standard indeterminacies in blind source separation and can be achieved if either sparseness or statistical independence constraints are imposed on $\mathbf{S}$. These constraints however do not hold in a number of real world scenarios. In this paper we exploit inherent 3D tensorial structure of the multi-spectral image $\underline{\mathbf{X}}\in R_+^{I_1\times I_2\times I_3}$ with elements $x_{i_1 i_2 i_3}$ where $i_1=1,...,I_1$, $i_2=1,...,I_2$, $i_3=1, ...,I_3$. Each index is called way or mode and number of levels on one mode is called dimension of that mode. Multi-spectral image is a set of I_3 spectral band images with the size of $I_1\times I_2$ pixels. In this paper, and for the purpose of multi-spectral image decomposition, we adopt two widely used 3D tensor models: Tucker3 model and PARAFAC/CANDECOMP model. The Tucker3 model is defined as

$$\hat{\underline{\mathbf{X}}} = \underline{\mathbf{G}} \times_1 \mathbf{A}^{(1)} \times_2 \mathbf{A}^{(2)} \times_3 \mathbf{A}^{(3)} \tag{2}$$

where $\underline{\mathbf{G}} \in R_+^{J_1\times J_2\times J_3}$ is core tensor and $\left\{\mathbf{A}^{(n)} \in R_+^{I_n\times J_n}\right\}_{n=1}^{3}$ are factors and $\times_n$ denotes n-mode product of a tensor with a matrix $\mathbf{A}^{(n)}$. The result of $\underline{\mathbf{G}}\times_n \mathbf{A}^{(n)}$ is a tensor of the same order as $\underline{\mathbf{G}}$ but the size J_n replaced by I_n. PARAFAC model is a special case of Tucker3 model when $\underline{\mathbf{G}}$ is superdiagonal tensor with all elements zero except those for which all indices are the same. Compared to PARAFAC, Tucker3 model is more flexible due to the core tensor $\underline{\mathbf{G}}$ which allows interaction between a factor with any factor in the other modes. In PARAFAC model factors in different mode can only interact factor-wise. However, this restriction enables uniqueness of tensor factorization based the PARAFAC model within the permutation and scaling indeterminacies of the factors under very mild conditions and without need to impose any special constraints on them such as sparseness or statistical independence. Assuming $J_1=J_2=J_3=J$, we can also express *3*-mode flattened version of tensor $\underline{\mathbf{X}}$, this is matrix $\mathbf{X}_{(3)}$, in terms of *3*-mode flattened core tensor $\underline{\mathbf{G}}$, this yields matrix $\mathbf{G}_{(3)} \in R_+^{J\times JJ}$, and array factors $\left\{\mathbf{A}^{(n)}\right\}_{n=1}^{3}$ as [8]:

$$\mathbf{X}_{(3)} \approx \mathbf{A}^{(3)}\mathbf{G}_{(3)}\left[\mathbf{A}^{(2)} \otimes \mathbf{A}^{(1)}\right]^{\mathrm{T}} \tag{3}$$

where ⊗ denotes Kronecker's product. Hence, from flattened version of the Tucker3 model (3) and LMM (1) matrix of spectral profiles and tensor of spatial distributions of the materials are identified as

$$\mathbf{A} \leftrightarrow \mathbf{A}^{(3)}$$
$$\underline{\mathbf{S}} \leftrightarrow \underline{\mathbf{G}} \times_1 \mathbf{A}^{(1)} \times_2 \mathbf{A}^{(2)} = \underline{\mathbf{X}} \times_3 \left(\mathbf{A}^{(3)}\right)^{\dagger} \tag{4}$$

where $\underline{\mathbf{S}} \in R_{+}^{I_1 \times I_2 \times J}$ and $\left(\mathbf{A}^{(3)}\right)^{\dagger}$ denotes Moore-Penrose pseudo-inverse of $\mathbf{A}^{(3)}$. Second part of expression for $\underline{\mathbf{S}}$ is less sensitive to numerical errors than first part due to the fact that only one reconstructed quantity, array factor $\mathbf{A}^{(3)}$, takes places into reconstruction of $\underline{\mathbf{S}}$. Equivalence between mixing matrix $\mathbf{A}$ and array factor $\mathbf{A}^{(3)}$ can be used for blind extraction of the tensor $\underline{\mathbf{S}}$ without need to actually execute 3D tensor factorization. Mixing matrix can be estimated from the flattened version $\mathbf{X}_{(3)}$ of the image tensor $\underline{\mathbf{X}}$ by means of data clustering. Afterwards, tensor $\underline{\mathbf{S}}$ is obtained through *3*-mode multiplication of the multi-spectral image tensor $\underline{\mathbf{X}}$ and Moore-Penrose pseudo-inverse of $\mathbf{A}$. Presuming sparseness between spatial distributions of the materials and using linear mixture model (3) the following approximation holds

$$\mathbf{X}_{(3)}(:,i) \approx \mathbf{a}_j s_{j,i} \quad j \in \{1,...,J\}, \quad i \in \{1,...,I_1 I_2\} \tag{4}$$

i.e. pixels in the MSI, which are column vectors of data matrix $\mathbf{X}_{(3)}$, coincide with some of the columns of $\mathbf{A}$ depending on which material is present at the current pixels. Thus, $\mathbf{A}$ can be estimated from $\mathbf{X}_{(3)}$ employing some of standard data clustering algorithms, such as for example *k*-means algorithm [9]. It has been used in reported experiment. What is however of great importance for computational efficiency of proposed MSI decomposition scheme is that overall number of materials J is much less than overall number of pixels, i.e. $J << I_1 I_2$. Hence, only a small fraction of the overall number of pixels should be selected randomly to estimate $\mathbf{A}$. Presuming that pixel indexes are uniformly distributed, minimal number of pixels to be selected, $N_{\min}$, is limited from below by the smallest area, O, occupied by some material:

$$N_{\min} \geq \frac{I_1 I_2}{O} \tag{5}$$

To estimate the number of materials J present in the MSI mixing vectors that lie in 3D on the unit semi-sphere are parameterized as, [10]:

$$\mathbf{a}_j = [\cos(\varphi_j)\sin(\theta_j) \;\; \sin(\varphi_j)\sin(\theta_j) \;\; \cos(\theta_j)]^{\mathrm{T}}, \tag{6}$$

where φ_m and θ_m represent azimuth and elevation angles respectively that are confined in the interval $[0, \pi/2]$. By assuming *1*-dimensional concentration subspaces the clustering algorithm is outlined by the following steps, [10,11]:

1) We remove all data points close to the origin for which applies: $\left\{\|\mathbf{x}(t)\|_2 \leq \varepsilon\right\}_{t=1}^{I_1 I_2}$, where ε represents some predefined threshold. This corresponds to the case when all materials are close to zero.

2) Normalize to unit ℓ_2 norm remaining data points $\mathbf{x}(t)$, i.e., $\left\{\mathbf{x}(t) \leftarrow \mathbf{x}(t) / \|\mathbf{x}(t)\|_2\right\}_{t=1}^{I}$, where $I \leq I_1 I_2$ denotes number of data points that remained after elimination process.

3) Calculate function $f(\mathbf{a})$, where $\mathbf{a}$ is defined with (6):

$$f(\mathbf{a}) = \sum_{t=1}^{I} \exp\left(-\frac{d^2(\mathbf{x}(t), \mathbf{a})}{2\sigma^2} \right) \tag{7}$$

where $d(\mathbf{x}(t), \mathbf{a}) = \sqrt{1 - (\mathbf{x}(t) \cdot \mathbf{a})^2}$ and $(\mathbf{x}(t) \cdot \mathbf{a})$ denotes inner product. Parameter σ in (7) is called dispersion. If set to sufficiently small value, in our experiments this turned out to be $\sigma \approx 0.05$, the value of the function $f(\mathbf{a})$ will approximately equal the number of data points close to **a**. Thus, by varying mixing angles $0 \le \varphi, \theta \le \pi/2$ we effectively cluster data.

4) Number of peaks of the function $f(\mathbf{a})$ corresponds with the estimate of the number of materials J. Locations of the peaks correspond with the estimates of the mixing angles $\left\{ \left(\hat{\varphi}_j, \hat{\theta}_j \right) \right\}_{j=1}^{J}$, i.e., mixing vectors $\left\{ \hat{\mathbf{a}}_j \right\}_{j=1}^{J}$, where $\hat{\mathbf{a}}_j$ is given with (6). Hence, at the end of data clustering phase estimates of the number of materials J and mixing matrix **A** are obtained. Alternatively, *k*-means clustering algorithm can be used to estimate the mixing matrix.

3. RESULTS

Figure 1 left shows RGB image with simple and known ground truth. It contains three materials and has been used to validate accuracy of proposed MSI segmentation algorithm. Figure 1 right shows high-intensity fluorescent RGB image of the protoporphyrin IX accumulated in the skin tumor. This image has been used to extract binary spatial maps of the tumor and surrounding healthy tissue that were served as ground truth for evaluation of the receiver-operating-characteristic (ROC) curves for spatial maps of the tumor shown in Figures 4b to 4d. Top row of the Figure 2 shows spatial maps of materials extracted from RGB image shown in Figure 1 left by means of proposed algorithm that combines data clustering and *3*-mode multiplication of the MSI tensor and inverse of the estimated mixing matrix. Bottom row of the Figure 2 shows spatial maps obtained by applying second order non-negative matrix factorization (SO NMF) algorithm, [12], to LMM (1) of the MSI. Since materials in the experimental RGB image do not overlap in spatial domain we can evaluate performance of the employed blind image decomposition methods via the correlation matrix defined as $\mathbf{G}=\mathbf{S}\mathbf{S}^{\mathrm{T}}$. For the perfect separation the correlation matrix should be diagonal. Hence, separation performance can be measured as deviation from diagonal matrix. To quantify decomposition quality numerically we compute the correlation index in dB scale as

$$CR = -10 \log_{10} \sum_{\substack{i,j=1 \\ j \neq i}}^{M} g_{ij}^2 \tag{6}$$

where before calculating correlation matrix **G** rows of **S** are normalized to unit ℓ_2 norm. To make the extracted spatial maps of the materials visually comparable we have rescaled each extracted material to the interval [0, 1], wherein 0 represents the absence of the material and 1 represents the presence of the material. Hence, quality of the image decomposition is visible immediately. Average *CR* performance for results shown in top row of Figure 2 is 18.67 dB and for results shown in bottom row of Figure 2 is 4.26 dB. Figure 3 shows clustering function (7) in the mixing angles domain that is associated with Figure 1 left. Three peaks confirm existence of three materials in the experimental RGB image.

Figure 4a shows the weak-intensity RGB fluorescent image of the protoporphyrin IX accumulated in the skin tumor. It has been an input to blind decomposition methods. Decomposition results obtained by: tensor-based representation and clustering, matrix factorization based methods: SO NMF and dependent

component analysis (DCA) algorithm based on innovations representation, [13, 5], are respectively shown in Figures 4b to 4d. Corresponding receiver-operating-characteristic (ROC) curves are shown in Figure 5. Performance of proposed algorithm is better than SO NMF and DCA algorithms. Due the fact that clustering has been performed on 100 randomly selected pixels only, the computational efficiency was very high. All algorithms were implemented in MATLAB on a 2.4 GHz Intel Core 2 Quad Processor Q6600 based desktop computer with 4GB RAM. Computation times for clustering based NTF-like method, SO NMF algorithm and DCA algorithm are respectively given as: 0.2s, 30s and 3.6s.

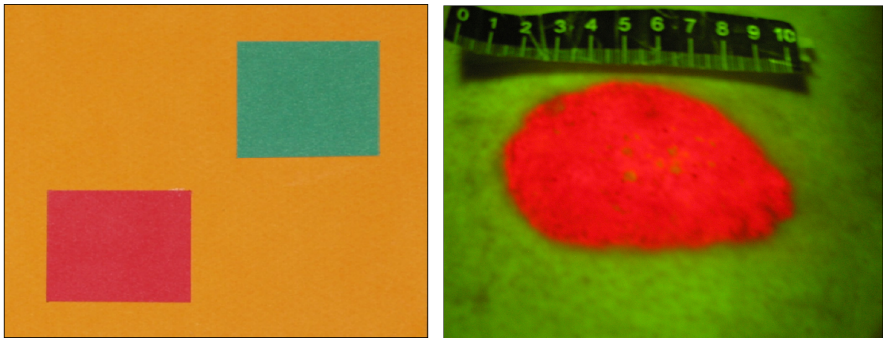

Fig. 1. left: RGB image with three materials; right: high-intensity fluorescent RGB image of the skin tumor.

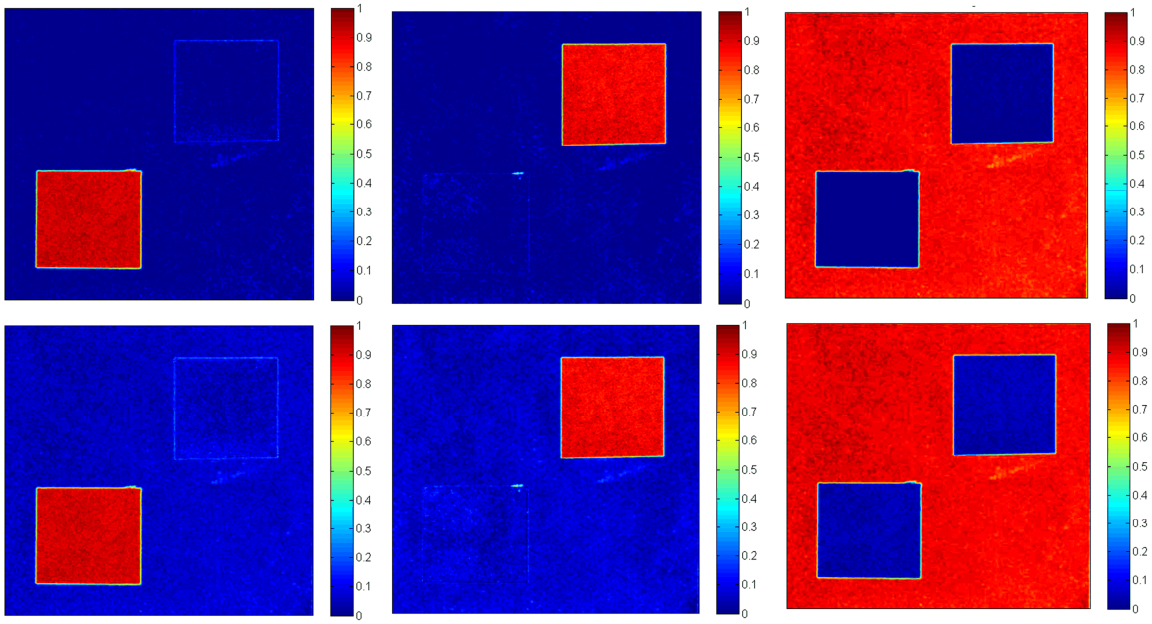

Fig. 2. Spatial maps of the tumor extracted from RGB image shown in Figure 1 left. Top row: tensor-based representation and clustering. Bottom row: SO NMF algorithm. Extracted spatial maps were rescaled to the interval [0, 1] and shown it in pseudo color scale, wherein dark blue color represents 0, i.e. the absence of the material, and dark red color represents 1, i.e. the presence of the material.

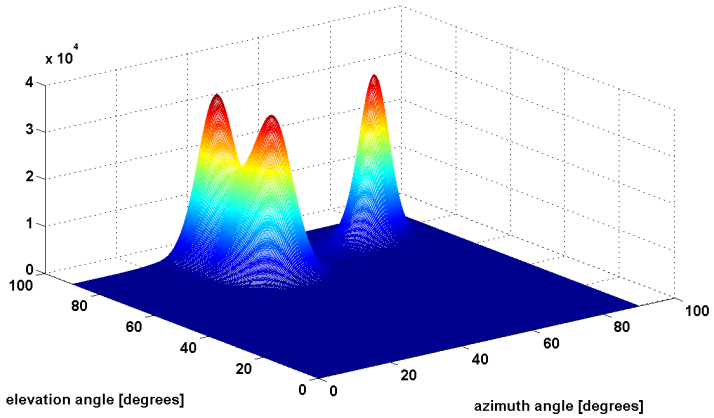

Figure 3. Clustering function associated with the experimental RGB image shown in Figure 1 left. Three peaks/clusters confirm existence of three materials present in the RGB image.

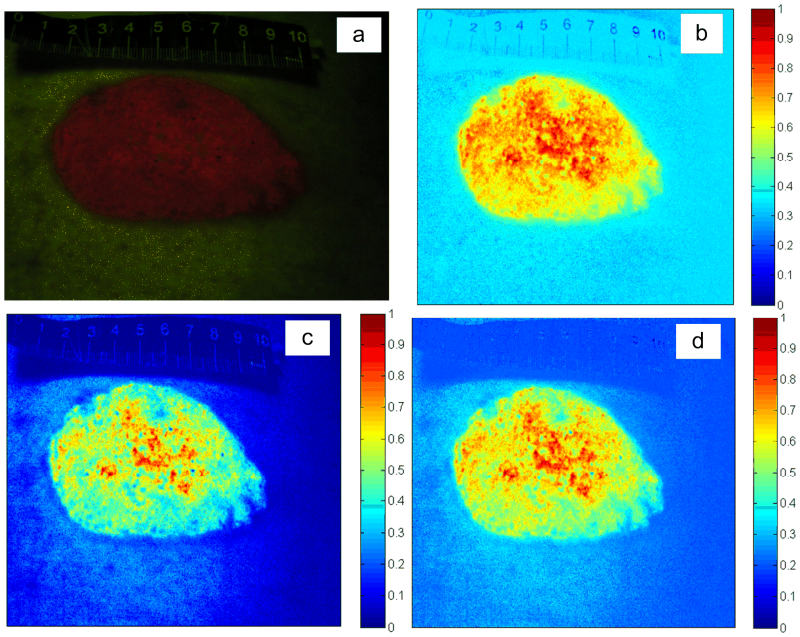

Fig. 4. (a) Low-intensity fluorescent RGB image of the tumor. (b) to (d) Spatial maps of the tumor extracted from RGB image shown in Figure 4a by means of: b) tensor-based representation and clustering; c) SO NMF algorithm; d) DCA algorithm based on innovations representation. Extracted spatial maps were rescaled to the interval [0, 1] and shown it in pseudo color scale, wherein dark blue color represents 0, i.e. the absence of the tumor, and dark red color represents 1, i.e. the presence of the tumor.

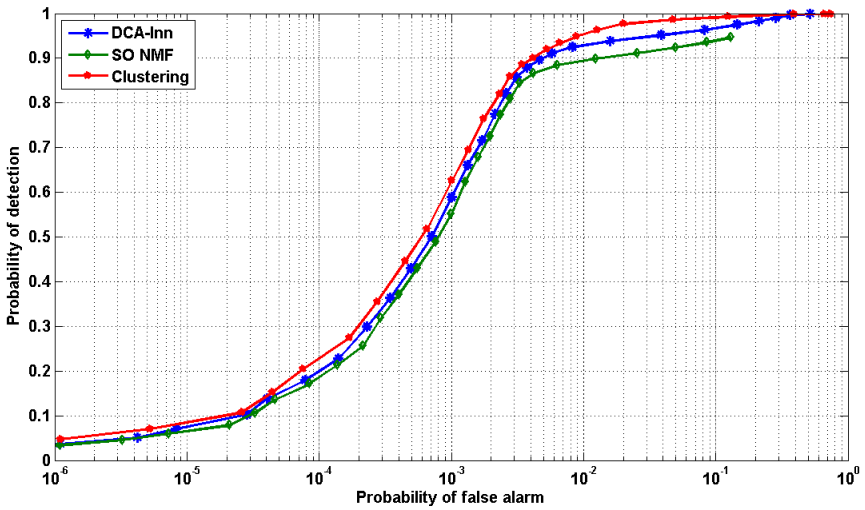

Fig. 5. ROC curves calculated for spatial maps of the tumor shown in Figures 4b to 4d: blue '*' - innovations based DCA algorithm; green diamonds - SO NMF algorithm; red stars - tensor-based clustering algorithm.

4. CONCLUSION

Novel approach to blind decomposition of multi-spectral fluorescent image for tumor demarcation is presented. It exploits tensorial structure of the image. Matrix of spectral profiles of the materials present in the image is estimated by means of data clustering using matricized version of the image. 3D tensor of spatial distributions of the materials present in the image is obtained through *3*-mode multiplication of the multi-spectral image tensor and inverse of the matrix of spectral profiles. Tensor representation of the multi-spectral image preserves its local spatial structure that is lost, due to vectorization process, when matrix factorization-based decomposition methods (such as non-negative matrix factorization and independent component analysis) are used. Due to presumed sparseness between the materials present in the image mixing matrix is identified by means of data clustering algorithm on a small number of randomly selected pixels. Superior performance of the tensor-based image decomposition over matrix factorization-based decompositions is demonstrated on experimental RGB image with known ground truth as well as on low-intensity multi-spectral fluorescent images of skin tumor.

ACKNOWLEDGEMENTS

The work of I. Kopriva and A. Peršin has been supported through grant 098-0982903-2558 funded by the Ministry of Science, Education and Sports, Republic of Croatia.

REFERENCES

[1] English, D.R., Armstrong, B.K., Kicker, A. and Fleming, C., "Sunlight and cancer," Cancer Causes Control 8, 271-283 (1997).

[2] Ericson, M.B., Sandberg, C., Gudmundson, F., Rosén, A., Larkö, O. and Wennberg, A.M., "Fluorescence contrast and threshold limit: implications for photodynamic diagnosis of basal cell carcinoma," J. Photochem. Photobiol. B: Biol. 69, 121-127 (2003).

[3] Scott, M.A., Hopper, C., Sahota, A., Springett, R., Mcllroy, B.W., Bown, S.G. and. MacRobert, A.J., "Fluorescence Photodiagnostics and Photobleaching Studies of Cancerous Lesions using Ratio Imaging and Spectroscopic Techniques, Lasers Med Sci 15, 63-72 (2000).

[4] Fischer, F., Dickson, E.F., Pottier, R.H. and Wieland, H., "An Affordable, Portable Fluorescence Imaging Device for Skin Lesion Detection Using a Dual Wavelength Approach for Image Contrast Enhancement

and Aminolaevulinic Acid-induced Protoporphyrin IX. Part. I Design, Spectral and Spatial Characteristics," Lasers Med Sci 16, 199-206 (2001).

[5] Kopriva, I., Peršin, A., "Unsupervised decomposition of low-intensity low-dimensional multi-spectral fluorescent images for tumour demarcation", Medical Image Analysis 13, 507-518 (2009).

[6] Kopriva, I. and Cichocki, A., "Blind Multi-spectral Image Decomposition by 3D Nonnegative Tensor Factorization", Optics Letters 34, 2210-2212 (2009).

[7] L. R. Tucker, "Some mathematical notes on three-mode factor analysis," Psychometrika 31, 279-311 (1966).

[8] Kim, Y. D., Cichocki, A. and Choi, S., "Nonnegative Tucker Decomposition with Alpha-Divergence," Proc. of the 2008 IEEE International Conference on Acoustics, Speech and Signal Processing (ICASSP), 1829-1832 (2008).

[9] Bishop, C.M., [Pattern Recognition and Machine Learning], Springer, 423-460 (2006).

[10] Kopriva, I., Cichocki, A., "Blind decomposition of low-dimensional multi-spectral image by sparse component analysis," Journal of Chemometrics, DOI: 10.1002/cem.1257.

[11] Naini, F.M., Mohimani G.H., Babaie-Zadeh M. and Jutten C., "Estimating the mixing matrix in Sparse Component Analysis (SCA) based on partial *k*-dimensional subspace clustering," Neurocomputing 71, 2330-2343 (2008).

[12] Zdunek, R., Cichocki, A., "Nonnegative matrix factorization with constrained second-order optimization," Signal Processing 87, 1904-1916 (2008).

[13] Hyvärinen, A., "Independent component analysis for time-dependent stochastic processes," Proc. of the International Conference on Artificial Neural Networks (ICANN'98), 541-546 (1998).